Anatomizing deformation mechanisms in nanocrystalline $Pd_{90}Au_{10}$

M. Grewer[a,*], C. Braun[a], M.J. Deckarm[a], J. Lohmiller[b], P.A. Gruber[b], V. Honkimäki[c], R. Birringer[a]

[a] *Experimentalphysik, Universität des Saarlandes, Saarbrücken, Germany*
[b] *Institute for Applied Materials, Karlsruhe Institute of Technology, Karlsruhe, Germany*
[c] *Materials Science Group, European Synchrotron Radiation Facility, Grenoble, France*

arXiv:1408.5049v3 [cond-mat.mtrl-sci] 1 Mar 2016

Abstract

We utilized synchrotron-based in-situ diffraction and dominant shear deformation to identify, dissect, and quantify the relevant deformation mechanisms in nanocrystalline $Pd_{90}Au_{10}$ in the limiting case of grain sizes at or below 10 nm. We could identify lattice and grain boundary elasticity, shear shuffling operating in the core region of grain boundaries, stress driven grain boundary migration, and dislocation shear along lattice planes to contribute, however, with significantly different and nontrivial stress-dependent shares to overall deformation. Regarding lattice elasticity, we find that Hookean linear elasticity prevailed up to the maximal stress value of ≈ 1.6 GPa. Shear shuffling that propagates strain at/along grain boundaries increases progressively with increasing load to carry about two thirds of the overall strain in the regime of macroplasticity. Stress driven grain boundary migration requires overcoming a threshold stress slightly below the yield stress of ≈ 1.4 GPa and contributes a share of $\approx 10\,\%$ to overall strain. Appreciable dislocation activity begins at a stress value of ≈ 0.9 GPa to then increase and eventually propagate a maximal share of $\approx 15\,\%$ to overall strain. In the stress regime below 0.9 GPa, which is characterized by a markedly decreasing tangent modulus, shear shuffling and lattice- and grain boundary elasticity operate exclusively. The material response in this regime seems indicative of nonlinear viscous behavior rather then being correlated with work- or strain hardening as observed in conventional fcc metals.

Keywords: deformation mechanisms, grain boundaries, mechanical testing, metallic material

1. Introduction

When substantially reducing the crystallite (grain) size D of polycrystalline metals into the nanometer regime, they show superior strength and hardness and are so potential candidate materials for a variety of applications. Over the last decade, this has motivated intense research efforts with the aim of gaining insight into the physics of grain size-dependent deformation mechanisms of nanocrystalline (NC) metals. Since the volume fraction of grain boundaries (GB) scales with the reciprocal grain size, the abundance of GBs at the nanometer scale supplies barriers for intergranular slip and the nanometer-sized grains entail a reduced capacity of dislocation generation and interaction even at the upper limit of the nanometer scale of ≈ 100 nm. As a consequence, higher strength, lower activation volume, and higher strain-rate sensitivity have been observed [1, 2]. With decreasing the grain size to the lower end of the nanoscale ($D \approx 10$ nm or below), it is expected that intragranular crystal plasticity becomes gradually or even dominantly replaced by GB-mediated deformation processes.

Simulations and experiments unraveled a variety of modes of plastic deformation related to GBs. So far the following processes have been identified: GB slip and sliding [3, 4, 5], stress-driven GB migration (SDGBM) coupled to shear deformation and grain rotation [6, 7, 8], as well as shear transformation (ST) mediated plasticity [9, 10], usually observed in glasses or colloidal systems [11], but here operating in the

*Corresponding author
Email address: micromanu@gmx.de (M. Grewer)

confined space related to the core region of GBs. Moreover, GBs and triple junction lines, locations where typically three GBs meet, may act as stress concentrators [12, 13], so effectively reducing the barrier for partial dislocation nucleation and emission. One of the intriguing aspects is that plastic deformation of NC metals requires that this variety of strain carriers interact in a synergistic way to make deformation happen in a compatible manner.

In a recent work Ames et al. [14] demonstrated that NC $Pd_{90}Au_{10}$ ($D \leq 10\,\mathrm{nm}$) exhibits a pronounced strain-rate dependence prevailing up to large strains. Utilizing activation parameters to identify active deformation mechanisms, they found the measured activation volume and strain-rate sensitivity of NC $Pd_{90}Au_{10}$ ($D \leq 10\,\mathrm{nm}$) to be compatible within the error margins with partial dislocation activity (PDA), STs (the generic flow event in metallic glasses) and SDGBM. Discrimination between just possible and relevant deformation mechanisms yet requires additional information. In a follow-up study, Grewer et al. [15] analyzed the activation energy of deformation in NC $Pd_{90}Au_{10}$ ($D \leq 10\,\mathrm{nm}$) and studied SDGBM in detail. They concluded that ST-based shear shuffling operating in GBs dominates the overall deformation behavior. More fundamentally, they found that the activation energy ΔG exhibits a barrier height scaling $\Delta G \propto \tau^{3/2}$ which bears great similarity with the Johnson-Samwer [16] universal scaling law of yielding in metallic glasses; τ is a measure of the applied load here. Finally, Skrotzki et al. [17] studied texture formation in NC $Pd_{90}Au_{10}$ induced by high-pressure torsion to find absence of any texture formation up to applied strains of $\gamma \approx 1$. Moreover, they observed that twinning and stacking fault formation is basically missing in this strain regime. Consequently, dislocation activity seems to play a minor role at the low end of the nanoscale.

Because of the complex interplay of disparate mechanisms, operating either sequentially or simultaneously, it remains to be clarified which role they play in responding to the intrinsic stress field and quantified which share to overall strain propagation is carried by them. Finding answers to these issues is a challenge for experiment and theory, as well as computational simulations. The latter have contributed to an atomic-level understanding of how different plasticity mechanisms interact on the nanoscale [18, 19, 20, 21]. Clearly, the deformation of NC materials involves a broad spectrum of time and length scales beginning with the atomistic details of local shear in GBs, dislocation nucleation, -motion and -interaction, likewise, slip transfer across GBs to end in crack propagation or shear banding at the system level. Therefore, direct comparison between computer simulations and deformation experiments or advanced microscopy, as well as atom probe tomography still remains a tough case. Not least since the atomic interaction potentials used in simulation scenarios may not fully cover the genuine nature of the materials.

We address the experimental approach here and discuss which insight we gained from synchrotron-based diffraction measurements to in-situ study the microstructural evolution during deformation of NC $Pd_{90}Au_{10}$ specimens prepared in a specific sample geometry termed shear compression specimen (SCS) (details are given in section 2). In addition, we analyzed dark field transmission electron micrographs at different strain values to extract possible changes of the grain size distribution function caused by SDGBM. The paper is organized as follows: first, the experimental setup and measurement procedures are introduced. Secondly, we discuss how individual XRD peak parameters have been extracted from the in-situ experiment and relate them to microstructural changes as well as associated deformation mechanisms. We will use this information in conjunction with the data from mechanical testing to quantify the relative deformation share of each identified process as a function of applied strain. Eventually, we display the shares of mechanisms to overall deformation as a function of applied load to unravel their stress-dependent sequence and/or simultaneous onset and persistence as well as revealing possible synergistic effects associated with their simultaneous presence.

2. Material and Methods

Regarding the material system, we prepared NC $Pd_{90}Au_{10}$ alloys by inert-gas condensation (IGC) and compaction [22], allowing to explore grain sizes at or even below 10 nm. IGC-prepared NC materials are statistically isotropic (untextured) and homogeneous, characterized by a lognormal grain size distribution, and feature a GB-misorientation distribution that bears great similarity with the Mackenzie-distribution [23, 24, 17]. As such, they manifest a models system to the random polycrystal. Moreover, the PdAu alloy

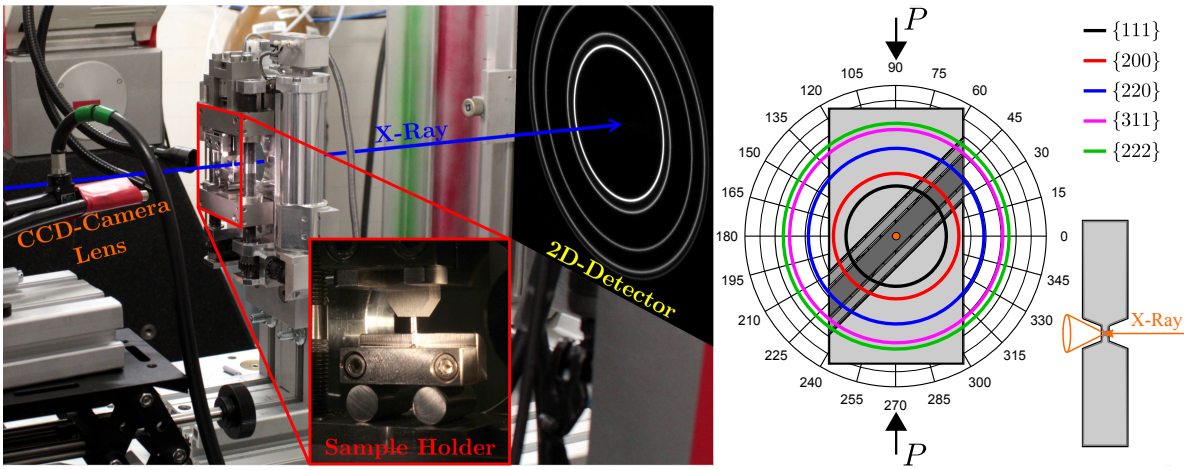

Figure 1: Photograph of the measurement setup at beamline ID15A at ESRF with the mechanical testing device mounted on top of a six axis goniometer. The inset shows a magnification of the compression stage with the roll bearing sample holder and a SCS in place. The sketch on the right displays a SCS in front and side view and serves as a reference frame for the polar plots shown throughout this document. In all cases the slit of the SCS is positioned 45° from lower left to upper right and load P is applied along the vertical direction ($\phi = 90°, 270°$). Furthermore, all graphs showing {hkl}-data will refer to the same color code as used for the Debye-Scherrer rings in this sketch. The smaller side view shows the trapezoid slit geometry enabling undisturbed propagation of the diffracted beam.

system is a fully miscible solid solution with a relatively high stacking fault energy $\approx 180\,\mathrm{mJm}^{-2}$ [25, 26] in the Pd-rich alloys. Applying a compaction pressure of 2 GPa, we produced disk-shaped samples (as prepared samples) with a diameter of 8 mm and a thickness in the range of 0.5-1.0 mm. The volume-weighted average grain-diameter $\langle D \rangle_{\mathrm{vol}}$ of the as prepared samples was determined from the Bragg peak broadening of X-ray diffraction (XRD) measurements using Klug & Alexander's [27, 28] modified Williamson-Hall technique. The diffraction experiments were performed on a laboratory diffractometer (PANalytical XPert Pro) operated in Bragg-Brentano focusing geometry and $\theta - \theta$ mode. The composition of as prepared specimens was determined by EDX in a SEM (JEOL F 7000).

Mechanical testing was carried out using small-scale-specimens having the specific geometry shown in Fig. 1. Such specimens are termed shear compression specimens (SCS) [29] and were fabricated by employing spark erosion processing to as prepared samples. The two parallel and oblique slits recessed on opposing faces form the gauge section. The dimensions of the SCS were 7 mm×0.95 mm×0.77 mm (H×W×T) and the gauge section was thinned to a thickness of 123 μm. Applying load to the top and bottom faces forces the SCS to shear along the gauge section, which has been oriented 45 ° relative to the load direction. Such miniaturized SCS have been successfully applied to large strain testing of NC PdAu alloys by Ames et al. [14]. Since plastic deformation is confined to the gauge section [30], the SCS is ideally suited for synchrotron based transmission experiments with the scattering vector probing the in-plane evolution of XRD peak parameters during deformation. To avoid shadowing of the scattering cones by the edges of the gauge slits, we deviate from the SCS design in [14] by using a trapezoid slit profile (see Fig. 1) to adapt the geometry of the SCS to the diffraction measurement.

Figure 1 shows the experimental setup at the high energy microdiffraction endstation (HEMD) of beamline ID15A at the European Synchrotron Radiation Facility (ESRF). Mechanical testing was performed by a Kammrath & Weiss tension/compression device made up of two load plungers moving symmetrically towards the center, thus keeping the gauge section in fixed position relative to the incoming beam. The lower plunger was replaced by a roll bearing wagon to substantially reduce the friction coefficient of the horizontal sample movement that goes along with the enforced shear deformation [30]. The testing device with the installed SCS was mounted on top of a six axis goniometer, which enables exact placement of the sample with respect to the incoming synchrotron beam. The focused beam with a cross section of 8 μm × 20 μm was directed to the center of the thin gauge section, thus penetrating approximately 30 billion grains. The

high energy x-ray radiation had a wavelength of $\lambda = 0.178\,\text{Å}$ entailing an in-plane orientation (perpendicular to the incoming beam direction) of the scattering vector. The diffracted signal was recorded on a 2D-area detector (mar CCD), capable of recording one scan every seven seconds. The detector-sample distance was set to capture the first five Bragg reflections (Debye-Scherrer rings), so enabling a reasonable compromise between recording sufficiently high diffraction orders while still maintaining a good angular resolution. For data analysis, the 2D-scans were averaged over 2°-wide polar segments to give 180 radial line scans which where then fitted by Split-Pearson-VII functions to obtain peak parameters like 2θ peak-position, integral intensity and integral peak width. For more details related to data reduction, we refer to the recent work by Lohmiller et al. [31].

Sample deformation was recorded by a Pixelink CCD-camera using an inline microscope lens for magnification and several light sources to illuminate the sample. The images were processed by digital image correlation (DIC) to extract true sample displacements to establish load-displacement curves. As the gauge section of the SCS deforms under dominant shear and some superimposed pressure, there are no simple formulas to compute stress-strain curves from load-displacement data. Instead, we employed finite element analyis (FEA) using Abaqus, adapted to each individual sample geometry, to first generate load-displacement curves that best approximated the experimental load-displacement curves. Based on these fits, Von Mises equivalent stress-strain curves were then straightforwardly obtained by FEA. More details on SCS-testing are given in [14, 30]. When placing the SCS samples in the sample holder, it needs some load until the SCS fully adapts to the frame of the testing machine. Such mounting problems generate uncertainties in the initial stage of the load displacement curves. To circumvent these uncertainties in the stress strain domain, we decided to extrapolate back from the clean linear stress strain regime to zero stress and strain. Therefore, this extrapolated regime (below about 0.3% strain) was not used for further analysis.

We also performed ex-situ TEM measurements on the deformed SCS to further characterize the evolution of the microstructure. Using focused ion beam (FIB) milling, thin lamellae were cut from the only elastically deformed bulk of the specimen as well as from the gauge section having experienced $\approx 32\,\%$ applied strain. The former serves as a reference for the undeformed material. The plastically deformed gauge lamella was oriented with its normal pointing perpendicular to the incoming x-ray beam direction. The grain microstructure of the lamellae were analyzed by an FEI-Titan TEM, operated in dark-field mode by using different portions of the {111}-diffraction ring. Multiple areas were analyzed on each lamellae. As standard contrast thresholding approaches for automated grain analysis do not work well on micrographs of NC samples, the images were processed manually in ImageJ [1]. For each visible grain the longest and shortest chord length was determined using the line measurement tool in ImageJ. A consistency check, involving the repeated measurement of an image set containing ca. 200 grains, showed good reproducibility of individual grain diameters within 0.5 nm uncertainty. To improve statistics and reduce the overall error, at least 1000 grains were counted per lamella (deformed and undeformed).

3. Results and Discussion

3.1. Mechanical testing

Figure 2 displays stress-strain curves of three $Pd_{90}Au_{10}$-SCS, deformed at a constant machine speed of $0.15\,\mu\text{m/s}$ which translates into applied strain rates $\dot{\varepsilon}_\text{a}$ between $1.1 \cdot 10^{-3}\,\text{s}^{-1}$ and $1.8 \cdot 10^{-3}\,\text{s}^{-1}$. Despite the slightly different applied strain rates (owing to small deviations in sample geometry), these curves not only demonstrate good reproducibility but also suggest that generic intrinsic material behavior is reflected in the stress-strain response rather than influence of extrinsic effects. This is also true for the scattering data collected during deformation. In what follows, we will therefore exemplarily discuss the diffraction results of the SCS marked by * in Fig. 2.

[1] rsbweb.nih.gov/ij/

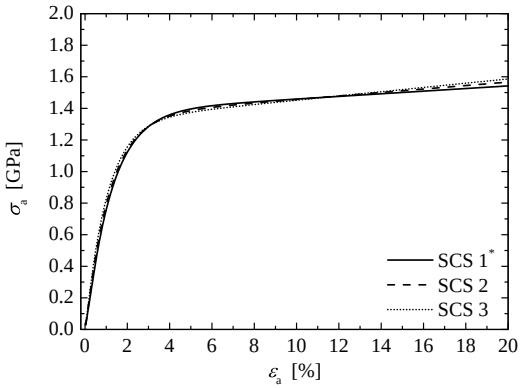

Figure 2: Stress-strain curves of three individual $Pd_{90}Au_{10}$-SCS deformed at $\dot{\varepsilon}_a \approx 1.5 \cdot 10^{-3}\,s^{-1}$. The * marks the sample that will be analyzed and discussed throughout this document.

3.2. Bragg-peak position and lattice strain

First, we look at the 2θ-angles characterizing the different {hkl}-Bragg peak positions. Using Bragg's law, it is straightforward to compute the corresponding lattice spacing $d_{hkl} = \lambda(2\sin\theta_{hkl})^{-1}$, where θ_{hkl} is half of the diffraction angle and λ=0.178 Å is the wavelength of the synchrotron radiation. During deformation the lattice spacings are expected to change so that the resulting elastic lattice strain ε_{hkl} can be extracted from

$$\varepsilon_{hkl} = \frac{\Delta d_{hkl}}{d_{hkl,0}} = \frac{\sin\theta_{hkl,0}}{\sin\theta_{hkl}} - 1, \tag{1}$$

where $\Delta d_{hkl} = d_{hkl} - d_{hkl,0}$ and the index $_0$ corresponds to values of the initially undeformed sample. This definition implies positive lattice strain with increasing lattice spacing (tension), while a decrease (compression) leads to negative strain values. A polar plot of absolute values of the {111}-lattice strain of a NC $Pd_{90}Au_{10}$-SCS is displayed in Figure 3(a) for several selected deformation states. The large maxima along the vertical load direction correspond to negative compressive strains, while the smaller horizontal

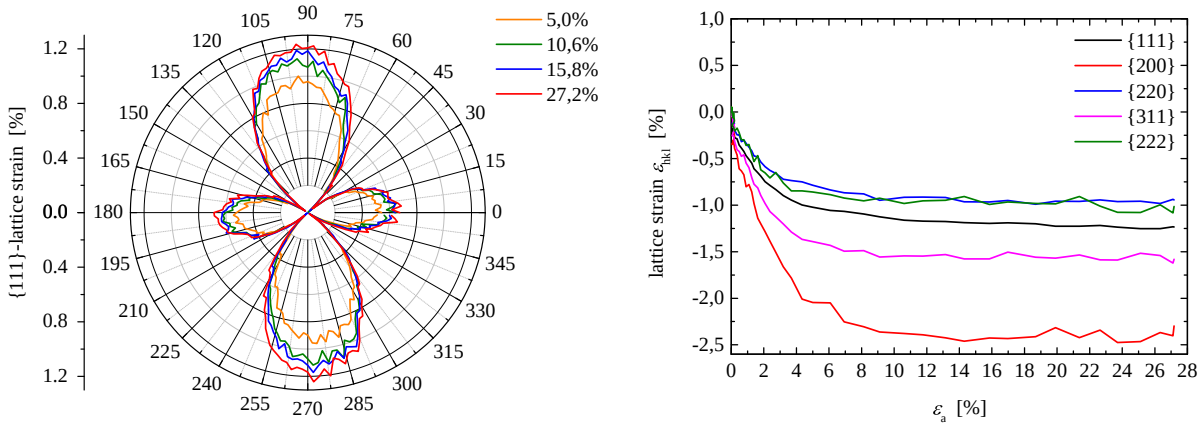

Figure 3: (a) Polar plot of absolute values of the {111}-lattice strain of four selected deformation states as indicated in the figure legend. Horizontal loops correspond to lateral tension (positive lattice strain according to Eq. 1), whereas the vertical loops are due to lattice compression (negative strain) (b) Compressive lattice strains of different {hkl}-lattice planes as a function of applied strain ε_a evaluated along the load direction ($\phi = 90°, 270°$).

maxima are positive strains due to lateral tension. As the scattering vector is oriented perpendicular to the

diffracting lattice planes, the signal along the load direction corresponds to a stack of horizontally oriented {111}-lattice planes and likewise for higher diffraction orders. Interestingly, the maximal strain values are not observed exactly along the load direction ($\phi = 90°, 270°$) but at $\phi = 95°, 275°$ instead. In fact, the whole graph appears to be rotated $\approx 5°$ counterclockwise, indicating a transformation of the external load state, which, as can be verified by FEA, is related to the specific sample geometry (see sketch in Fig. 1).

Clearly, increasing load and hence applied strain correlate with increasing lattice strain, either compressive or tensile. In Fig. 3(b), we show the compressive lattice strain ε_{hkl} of all five measured Bragg reflections as a function of applied strain ε_a, evaluated along the load direction ($\phi = 90°$, $\phi = 270°$). Due to the elastic anisotropy of PdAu, lattice planes with different Miller indexes experience different magnitudes of lattice strain and, typical for face centered cubic (fcc) metals, the {200}-planes are elastically most compliant. Apart from the different magnitudes, the lattice strain development of all planes follows roughly the shape of the stress-strain curve. This behavior is not unexpected though, since the evolution of lattice strain essentially describes the elastic deformation of the myriad of nanometer-sized crystal lattices. Interestingly, when plotting the applied stress as a function of the absolute value of lattice strain $|\varepsilon_{hkl}|$ along the load direction, as shown in Fig. 4(a), a linear correlation between stress and strain is observed. This evidence implies that even at such high stress values ($\sigma_\mathrm{a} > 1.5\,\mathrm{GPa}$) nonlinear elastic behavior is absent but Hooke's law $\sigma_\mathrm{a} = C_{hkl}\,\varepsilon_{hkl}$, where C_{hkl} is the {hkl}-dependent elastic modulus, still applies. The only exception are the most compliant {200}-planes that slightly deviate from the straight line in Fig. 4(a), suggesting presence of nonlinear elastic contributions. Nevertheless, evaluation of the arithmetic mean of the slopes of the linear fits C_{hkl}, weighted by their lattice plane multiplicity factor, results in an effective Young's modulus $\langle C \rangle = 118 \pm 4\,\mathrm{GPa}$, that is remarkably close to the Young's modulus of coarse grained $Pd_{90}Au_{10}$, which was determined by ultrasound to give a value of $127 \pm 5\,\mathrm{GPa}$ [32]. We therefore think that the implicit assumption of a homogeneous mean stress equal to the applied stress is valid.

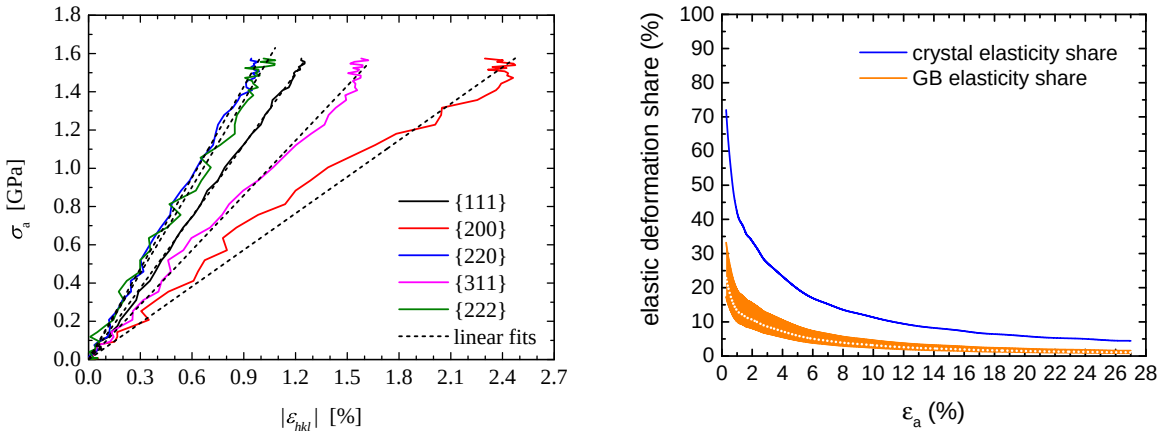

(a) (b)

Figure 4: (a) Applied stress σ_a as a function of the absolute value of lattice strain $|\varepsilon_{hkl}|$ along the load direction. Linear fits show that the elastic lattice deformation essentially follows Hook's law up to large stresses. Only the most compliant {200}-planes deviate from straight line behavior, indicating possible nonlinear elastic contributions. (b) Share of crystal lattice elasticity to overall deformation (blue). The orange ribbon represents the spread between the upper and lower bound values of the share of GB elasticity to overall deformation (see text for details). The dotted line indicates the share corresponding to the mean Young's modulus of upper und lower bound.

We now exploit the contributions of crystal- and GB elasticity to overall deformation. In mechanical equilibrium, the generalized capillary equation [33] prescribes that GB stresses are balanced by bulk stresses of the abutting crystallites. Therefore, we assume that crystal elasticity goes along with elastic behavior of GBs, which however have significantly reduced elastic moduli [34]. The total elastic strain, $\varepsilon_\mathrm{elastic}$, related

to the sample length measured along the loading direction, is then given by $\varepsilon_{\mathrm{elastic}} = (1-\chi)\varepsilon_{\mathrm{x}} + \chi\varepsilon_{\mathrm{GB}}$, where ε_{x} is the elastic strain due to crystal elasticity, and $\varepsilon_{\mathrm{GB}}$ is the strain contribution of the myriads of GBs occupying a length share χ. Consequently, $(1-\chi)$ represents the length share of crystallites along the loading direction. The parameter χ is directly connected with the grain size $\langle D\rangle_{\mathrm{vol}}$ and can be computed when the width σ of the grain size distribution and the structural width of the GBs, δ, is known [34, 32].

The value of ε_{x} can be straightforwardly approximated by setting $\varepsilon_{\mathrm{x}} = \langle\varepsilon_{\mathrm{hkl}}\rangle$, where the average elastic strain in loading direction $\langle\varepsilon_{\mathrm{hkl}}\rangle$ is represented by the arithmetic mean of the five curves displayed in Fig. 3(b), weighted by their respective x-ray lattice plane multiplicity factors. The GB elastic strain can not be extracted directly from diffraction data since the randomness of the interparticle interference generates a rather diffuse background intensity, which is in general not amenable to extract strain information. Therefore, we write an effective Hooke's law for the aggregate of GBs $\sigma_{\mathrm{a}} = \langle E_{\mathrm{GB}}\rangle\,\varepsilon_{\mathrm{GB}}$, where $\langle E_{\mathrm{GB}}\rangle$ is the effective Young's modulus of GBs and for the aggregate of crystallites $\sigma_{\mathrm{a}} = \langle C\rangle\,\varepsilon_{\mathrm{x}}$. Equating the right hand side of both Hooke's laws, we find the sought expression for $\varepsilon_{\mathrm{GB}} = \langle\varepsilon_{\mathrm{hkl}}\rangle(\langle C\rangle/\langle E_{\mathrm{GB}}\rangle)$.

The shares of the myriads of nanocrystals and GBs to overall strain ε_{a} can be deduced from

$$\frac{\varepsilon_{\mathrm{elastic}}}{\varepsilon_{\mathrm{a}}} = (1-\chi)\frac{\langle\varepsilon_{\mathrm{hkl}}\rangle}{\varepsilon_{\mathrm{a}}} + \chi\frac{\langle\varepsilon_{\mathrm{hkl}}\rangle}{\varepsilon_{\mathrm{a}}}\frac{\langle C\rangle}{\langle E_{\mathrm{GB}}\rangle}. \tag{2}$$

The first term on the right hand side of Eq. 2 represents the crystal elastic share to overall deformation and the second term accounts for the GB share. With $\sigma = 1.5$ (see Fig 8(a) and 8(b)) and $\delta = 0.76\pm0.01$ nm [32] , the evolution of the share of crystal elasticity as a function of increasing deformation can be computed and is shown in Fig. 4(b). To estimate the share of GB elasticity to overall deformation, we need to approximate the ratio $\langle C\rangle/\langle E_{\mathrm{GB}}\rangle$. To fix $\langle C\rangle$, we make use of the value $\langle C\rangle = 118 \pm 4$ GPa deduced from Fig. 4(a) and note that this value represents the effective Youngs's modulus of the aggregate of crystallites, which must be slightly larger then the true Reuss lower bound of the aggregate. We recently determined the effective (high frequency) Young's modulus of GBs by means of ultrasound measurements on unloaded samples to 61 ± 8 GPa [32]. However, under an applied load, we cannot rule out, even at the onset of deformation, configurational changes to occur in the core region of GBs that should give rise to an increase of $\langle E_{\mathrm{GB}}\rangle$. Thus, the zero-load high frequency Young's modulus manifests a lower bound to the effective GB modulus $\langle E_{\mathrm{GB}}\rangle$. For the sake of argument, we assume $\langle E_{\mathrm{GB}}\rangle = 61 \pm 8$ GPa, consequently, the share of strain of GBs to overall deformation assumes upper bound character. In contrast, an ultimate upper bound for $\langle E_{\mathrm{GB}}\rangle$ entails $\langle E_{\mathrm{GB}}\rangle = \langle C\rangle$, and so results in a lower bound for the GB share to overall deformation. The spread of the discussed bounds is indicated by the orange ribbon in Fig. 4(b). In what follows, we consider the share of GB elasticity to overall deformation corresponding to the mean Young's modulus of the upper- and lower bound, represented by the dotted line in Fig. 4(b).

3.3. Integral Peak Width: Microstrain and Grain Size Evolution

In this paragraph we focus on the evolution of the integral peak width of the diffraction reflexes (Debye-Scherrer rings). The two main factors that contribute to the broadening of diffraction peaks of a NC material are the small size of the scattering domains, i.e. small grain size, and the so called microstrain e. The latter arises from small variations in lattice spacings of neighboring grains, which are commonly attributed to strain fields near GBs or lattice distortions caused by stored dislocations [35]. However, virtual diffraction experiments in conjunction with molecular dynamics (MD) based determination of atomic level strains [36] have shown that the XRD microstrain is insensitive to strain fields that decay faster than $r^{-3/2}$, specifically, the exponentially decaying local strains near GBs. Instead, the microstrain broadening in NC materials in the limit of small grain sizes is dominated by long range displacement fields that extend throughout the grains and arise from compatibility constraints imposed on the grains to form a space filling tessellation of crystalline objects. In fact, studying room-temperature grain growth in NC Pd ($D_{\mathrm{initial}} \approx 10$ nm), Ames et al. [37] have found the XRD microstrain to be inversely proportional to the average grain size $e \propto 1/\langle D\rangle$, suggesting that microstrain is in fact related to tesselation constraints and therefore is a generic contribution in any polycrystalline material. Due to the $1/\langle D\rangle$-scaling, microstrain becomes particularly pronounced at the nanoscale even in an undeformed, load-free NC structure.

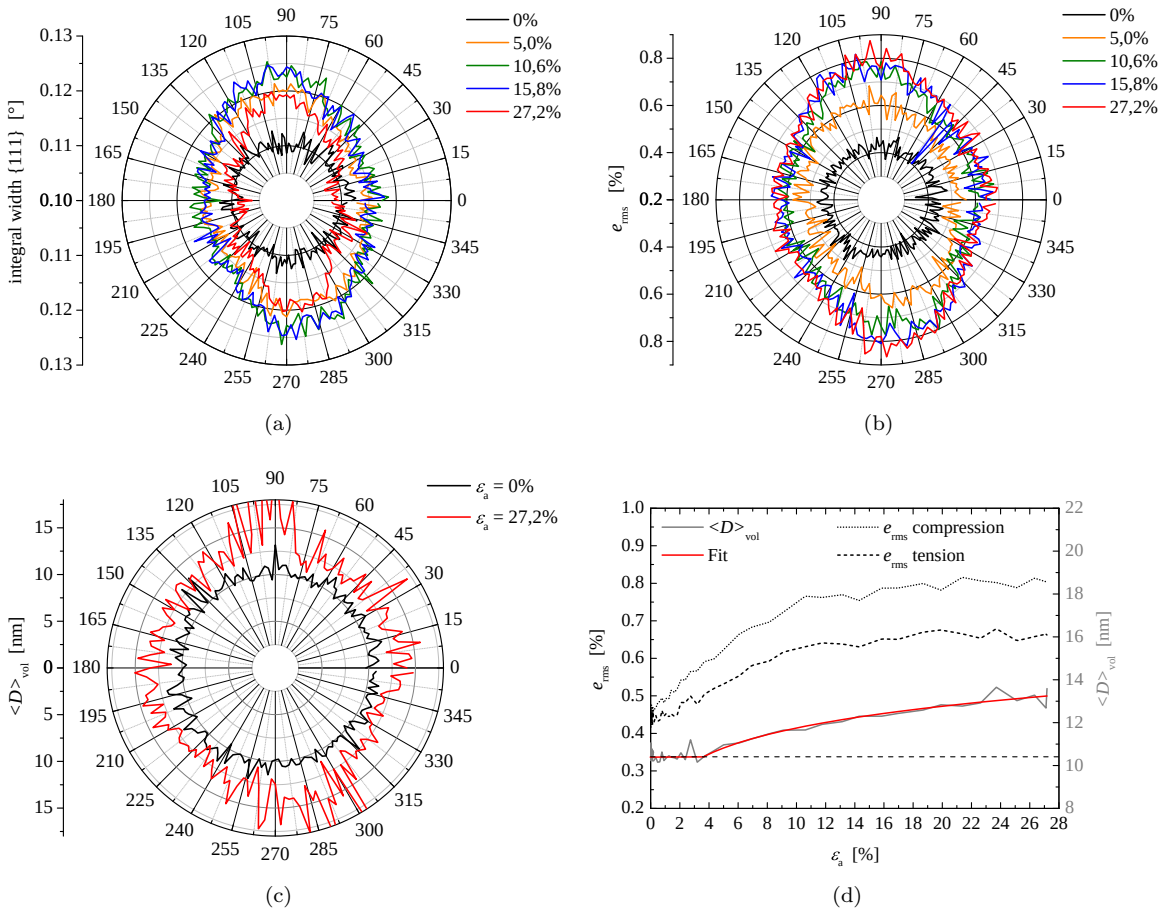

Figure 5: (a) Polar plot of the integral width of the {111} reflection for several deformation states. (b) Polar plot of the root mean square microstrain e_{rms}. (c) Polar plot of $\langle D\rangle_{\mathrm{vol}}$ for the initially undeformed SCS and at $\varepsilon_{\mathrm{a}} = 27.2\,\%$. (d) Evolution of $\langle D\rangle_{\mathrm{vol}}$ and e_{rms} as a function of applied strain. $\langle D\rangle_{\mathrm{vol}}$-values have been averaged over all polar angles (solid line) while microstrain values are shown for $\phi = 0\,^\circ$ (dashed line), corresponding to lateral tension, and $\phi = 90\,^\circ$ (dotted line), equivalent to the load direction.

Upon loading, the deduced microstrain also reflects the elastic anisotropy of the material, as grains with their hard axis being oriented parallel to the load direction will experience less compression than grains oriented along an elastically weaker axis. This behavior is readily illustrated by the polar plot in Fig. 5(a), where the integral {111}-peak width is increasing along the load direction with increasing strain up to $\varepsilon_{\mathrm{a}} = 15.8\,\%$. Further deformation to $\varepsilon_{\mathrm{a}} = 27.2\,\%$ leads to a decrease of the integral peak width, revealing a superimposed change of grain size. Effectively, the decreasing peak width is inversely proportional to the size of the scattering domains. Thus, the decrease of integral peak width at large strains in Fig. 5(a) can be attributed to an increase of the volume averaged grain size $\langle D\rangle_{\mathrm{vol}}$.

To analyze the microstrain and grain size evolution, we make use of the single line method, introduced by de Keijser et al. [38], which allows to extract separate values of grain size and microstrain for each {hkl}-reflection. The widely used Williamson-Hall approach led to poorly conditioned results, certainly due to the elastic anisotropy of PdAu but also related to the fact that the diffracted intensity has been recorded in transmission geometry, implying a slight variation of the orientation of the scattering vector with the diffraction angle which renders the Williamson-Hall approach intractable; further technical details can be found in [31]. Using the single line method, deconvolution of size and microstrain contributions results in

the following equations for the volume averaged grain size $\langle D\rangle_{\mathrm{vol}}$ and the microstrain e

$$\langle D\rangle_{\mathrm{vol}}^{hkl} = \frac{\lambda}{\beta_L \cos\theta_{hkl}} \quad (3)$$

$$e^{hkl} = \frac{\beta_G}{4\tan\theta_{hkl}}, \quad (4)$$

where β_L and β_G are the Lorentzian and Gaussian broadening shares as given in [38]. Analysis of the diffraction data related to the in-situ deformation of the investigated $Pd_{90}Au_{10}$-SCS delivers microstrain and volume averaged grain size values for the five measured diffraction orders. We compute the arithmetic mean of the individual {hkl}-dependent values to obtain the microstrain and $\langle D\rangle_{\mathrm{vol}}$ values displayed in Fig. 5(b) and 5(c), respectively. For convenience, we have converted e to the commonly used root mean square microstrain $e_{\mathrm{rms}} = (2/\pi)^{1/2}e$.

Initially, the microstrain is roughly 0.4 % along all polar angles. With increasing deformation, the microstrain steeply rises up to 0.8 % along the load direction and 0.65 % in the lateral tensile direction at $\varepsilon_{\mathrm{a}} = 10.6\,\%$. Further deformation does not yield a significant gain of microstrain. This becomes even more apparent in Fig. 5(d), where the evolutions of e_{rms} along the vertical compressive (dotted) and lateral tensile (dashed) direction are presented as a function of the applied strain. Interestingly, the elliptic shape of the microstrain polar plot corresponds well with the overall shape of the lattice strain development shown in Fig. 3(a). The obvious connection between lattice strain ε_{hkl} and microstrain e_{rms} corroborates the notion that microstrain in NC metals is essentially a measure of long range displacement fields originating from compatibility constraints. We cannot discriminate between possible additional microstrain contributions resulting from stress concentrators at triple junctions and bending of lattice planes both caused by the likely presence of GB-mediated deformation modes [39, 40].

Regarding grain size evolution, we first focus on the circular shape of the polar plot of the initial grain size (black) in Fig. 5(c). It indicates that the undeformed sample is made up of roughly equiaxed grains with a mean diameter of $\langle D\rangle_{\mathrm{vol}} = 10.4 \pm 0.7\,\mathrm{nm}$. This value is in close agreement with the grain size $\langle D\rangle_{\mathrm{vol}}^{\mathrm{IGC}} \approx 9\,\mathrm{nm}$ of the as prepared NC material, determined immediately after IGC by a Williamson-Hall analysis of XRD pattern recorded on an XPert Pro laboratory diffractometer in Bragg-Brentano focusing geometry, providing the required fixed orientation of the scattering vector. Therefore, we feel confident that the single line method is capable of catching the essential features of relative change of grain size.

In Fig. 5(d) the evolution of $\langle D\rangle_{\mathrm{vol}}$, averaged over all polar angles, is displayed as a function of the applied strain. Remarkably, the grain size remains nearly constant at $\langle D\rangle_{\mathrm{vol}} = 10.4\,\mathrm{nm}$ up to $\varepsilon_{\mathrm{a}} \approx 4\,\%$. Beyond that point grain growth is triggered and gradually advances with increasing plastic strain to reach a grain size of $\langle D\rangle_{\mathrm{vol}} = 13.4 \pm 2.7\,\mathrm{nm}$ at $\varepsilon_{\mathrm{a}} = 27.2\,\%$. The fact that grain size is still growing, while the microstrain values shown in Fig. 5(d) reach a plateau, is consistent with the decrease of the integral peak width in Fig. 5(a) beyond $\varepsilon_{\mathrm{a}} \approx 15.8\,\%$.

Comparing initial ($\langle D\rangle_{\mathrm{vol}} = 10.4 \pm 0.7\,\mathrm{nm}$) and final ($13.4 \pm 2.7\,\mathrm{nm}$) grain size values, we find that the deconvolution of microstrain and size broadening of pronouncedly stressed SCSs goes along with a higher error margin for the grain size values. Moreover, the deconvolution of size and strain seems severely affected by the high stress values along the vertical compressive direction (compare Fig. 5(b) and Fig. 5(c)) leading to a fictitious enhancement of size along the loading direction; we come back to this issue later. Accepting sources and margin of errors, the polar plot of the deformed state appears approximately circular implying that a possible evolution of grain shape anisotropy (growth texture) plays, if at all, a minor role. The observation that stress generates approximately *isotropic* growth seems to be indicative of stress driven grain boundary migration (SDGBM), synonymously termed coupled motion. Generally, it comprises the migration of a GB parallel and perpendicular to an applied shear stress τ. The coupling factor $\beta = v_{\parallel}/v_{\perp}$ [6] describes the ratio of migration parallel ($v_{\parallel}$) and perpendicular ($v_{\perp}$) to the applied stress in terms of the velocities v of the moving boundary. Since the NC samples prepared by IGC are statistically isotropic and homogeneous, we would expect that local migration anisotropies of individual boundaries should effectively average out. For the sake of argument, let us assume that the vertical compressive stress, generated by vertical loading of the SCS, delivers the maximal driving force (shear stress) for $v_{\perp}$ of appropriately oriented

GBs. We then expect GBs having normals aligned towards $\varphi \approx 180\,^\circ$ should exhibit maximal growth ($v_\perp$) along this direction. A faint signature related to this rationale may be seen in Fig. 5(c). On the other hand, we may consequently argue that the smaller but effective lateral tension should then lead to comparatively less growth along the load direction. This plausible reasoning is in contradiction to what has been extracted from experiment. Therefore, we are confident that the growth indicated along the load direction is in fact fictitious. What is more, SDGBM has been seen also in NC $Pd_{90}Au_{10}$ after high pressure torsion deformation [17]. A nearly doubling of grain size has been deduced, also based on x-ray Bragg-peak profile analysis, when the shear strain approached $\gamma \approx 0.5$. But no sign of concomitant texture formation could be observed, thus lending independent support to the assertion of isotropic growth.

Although it appears reasonable that SDGBM is the root cause of grain growth, we should not conceal that curvature-driven grain growth [37] and dislocation glide could also lead to changes in $\langle D \rangle_{\mathrm{vol}}$. However, the former process can be ruled out since all experiments were performed at room temperature (RT) and the microstructure of NC $Pd_{90}Au_{10}$ has been verified being stable (kinetically frozen) up to 60 °C. Loading the SCS and assuming availability of dislocations, unidirectional dislocation glide along the gauge section becomes favored and should manifest as grain shape anisotropy rather than isotropic grain growth. Specifically, assuming glide occurs on {111} lattice planes, it is implied then that such planes which are already oriented along the gauge section or rotate with increasing load towards this direction would experience the largest Schmid factor and should therefore be the most active glide planes. As a result, the grain chord length measured along the glide-plane normal should shrink and grain elongation should appear along the gauge section. In particular, we would expect a decrease in grain size in the angular regime around 135 ° and a concomitant increase towards $\approx 225\,^\circ$. However, such a behavior is not corroborated by experiment (Fig. 5(c)).

We might even argue that anisotropic growth related to both SDGBM and dislocation glide contributes in effect (due to their simultaneous presence) to apparent isotropic growth. However, as discussed above the leading orientation dependence of both effects is well within the resolution of experiment and, therefore, allows us to discriminate between simultaneous presence of both processes or contribution of a single process. Clearly, our experimental evidence reflecting that grain growth evolves basically grain-shape preserving favors SDGBM as the root cause of growth. Yet, this rationale relies upon the assumption that both processes contribute with well resolvable growth rates to overall growth. Therefore, to this end we cannot discard the presence of dislocation glide since its effect on grain-shape change may be so small that it is beyond the resolution associated with probing size by x-ray line broadening; we come back to this problem in the following section.

To estimate the contribution of SDGBM to overall strain, we refer to a simple model displayed in Fig. 6(a). We assume growth of the middle grain in response to the applied shear stress τ which induces a shear strain $\gamma = \Delta x/3D$. The shear strain can also be expressed as $\gamma = \beta \Delta D/3D$, where ΔD denotes the grain growth relative to the initial grain size D. Using the $\langle D \rangle_{\mathrm{vol}}$-data in Fig. 5(d), an average coupling factor of $\langle \beta \rangle = 0.3$ [41] and the relation $\varepsilon = \gamma/\sqrt{3}$, it is straightforward to compute the relative contribution $\varepsilon_{\mathrm{SDGBM}}/\varepsilon_{\mathrm{a}}$ of SDGBM as a function of applied strain. The resulting evolution of the SDGBM share is shown in Fig. 6(b) together with the value from the TEM analysis (see Fig. 8(a)), which we discuss in the following section. It should be noted that by letting both GBs move in opposite vertical and horizontal directions, as shown in Fig. 6(a), we estimate an upper bound for the associated shear strain.

3.4. Integral Scattering Intensity and Onset of Preferred Orientation Development

Before deformation, all {hkl}-reflections produced Debye-Scherrer rings of uniform intensity all around their circumference (Fig. 7(a)). This signature is typical for a material made up of randomly oriented grains. Upon loading, the measured intensities remain fairly constant initially, however, when strains larger than 10 % are reached, a subtle redistribution of scattering intensities is observed (see Fig. 7(b-d)). More specifically, a pseudo 6-fold symmetry associated with intensity maxima every 60 ° is found for the {111}- and {220}-reflections, while it is a pseudo 2-fold symmetry for the {200}-reflection. We note that the relative change of intensities $I_{\mathrm{hkl}}/I_{\mathrm{hkl,0}}$ related to the maxima of the rings is comparatively small, $I_{\mathrm{hkl}}/I_{\mathrm{hkl,0}} < 1.2$ (see Fig. 7(b-d)), so that associating true texture formation with it would by far overestimate cause and effect. Nevertheless, the circumferential variation of intensity along Debye-Scherrer rings (raw data) caused

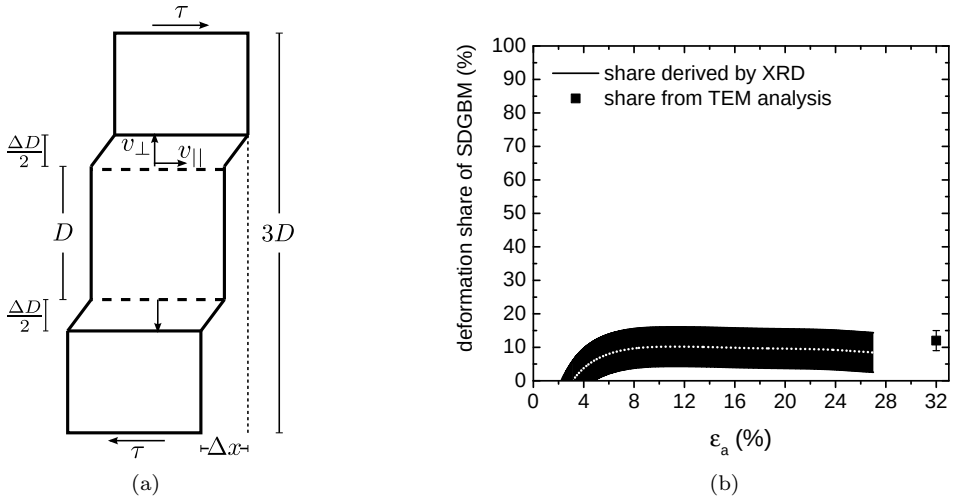

Figure 6: (a) Sketch to estimate the shear strain due to SDGBM. (b) Relative deformation share of SDGBM as a function of applied strain. The single square corresponds to the SDGBM share derived from the TEM grain size histograms shown in Fig. 8.

by deformation clearly indicates that grains have rotated into these new positions, which are close to the ideal texture components developing during simple shear of fcc metals. The analysis will be given in a separate paper.

We argue that the detection of the emergence of preferred grain orientations with such a high sensitivity is related to the SCS sample geometry in conjunction with the chosen diffraction set up. In fact, loading of SCS samples enforces simple shear along the gauge section and its effect is in-situ probed by high energy synchrotron radiation penetrating the entire gauge section. In the selected transmission geometry, due to the high monochromacy of radiation the scattering vector is oriented nearly perpendicular to the incoming beam direction (inclination: {111} 2.27 °, {220} 1.82 °, {200} 1.31 °) but otherwise unconstrained to probe all possible directions ($0° < \phi < 360°$) in the plane of the gauge section. Bragg reflection occurs whenever poles of {hkl}-lattice planes are oriented parallel to the scattering vector. The observation that increasing deformation generates a resolvable increase of intensity at a segment of the {111}-Debye-Scherrer ring centered around $\phi = 135\,°$ and $\phi = 315\,°$ clearly indicates that an increasing number of {111}-lattice planes must have oriented along the gauge section to accommodate the enforced unidirectional plane shear. Due to the symmetry of the fcc unit cell, additional intensity peaks corresponding to different possible orientations of {111}-planes within the unit cell are also generated and give rise to the observed six-fold intensity pattern. It seems plausible to assume that dislocation glide on {111}-planes and rotation of these slip planes to increasingly favorable positions where the resolved shear stress is highest are responsible for the discussed observations. The fact that we do not find sharp but broadened intensity peaks at the discussed polar angles (broadening $\Delta\phi \approx 30\,°$, Fig. 7(b)) appears reasonable since a combination of high enough local nucleation stress for dislocation emission and sufficient vicinity to the primary slip system with highest Schmid factor will eventually control deformation by slip. A validation of this conjecture yet requires a rigorous texture analysis. However, the unique geometry of the SCS in conjunction with the requirement that diffraction must be executed in transmission geometry, make it impossible to carry out the required rotations of the SCS which are inevitable to extract full texture information.

In a recent work, Skrotzki et al. [17] studied in great detail texture formation (Euler-space representation) in NC $Pd_{90}Au_{10}$ specimens after high pressure torsion (HPT) deformation. Applying HPT, the NC specimen is subjected to a compressive pressure of several GPa at room temperature and simultaneously to a torsional strain which is transmitted through rotation of the lower sample support. Surface frictional forces thus deform the disk shaped sample geometry by shear which is increasing along the radius and with the number of

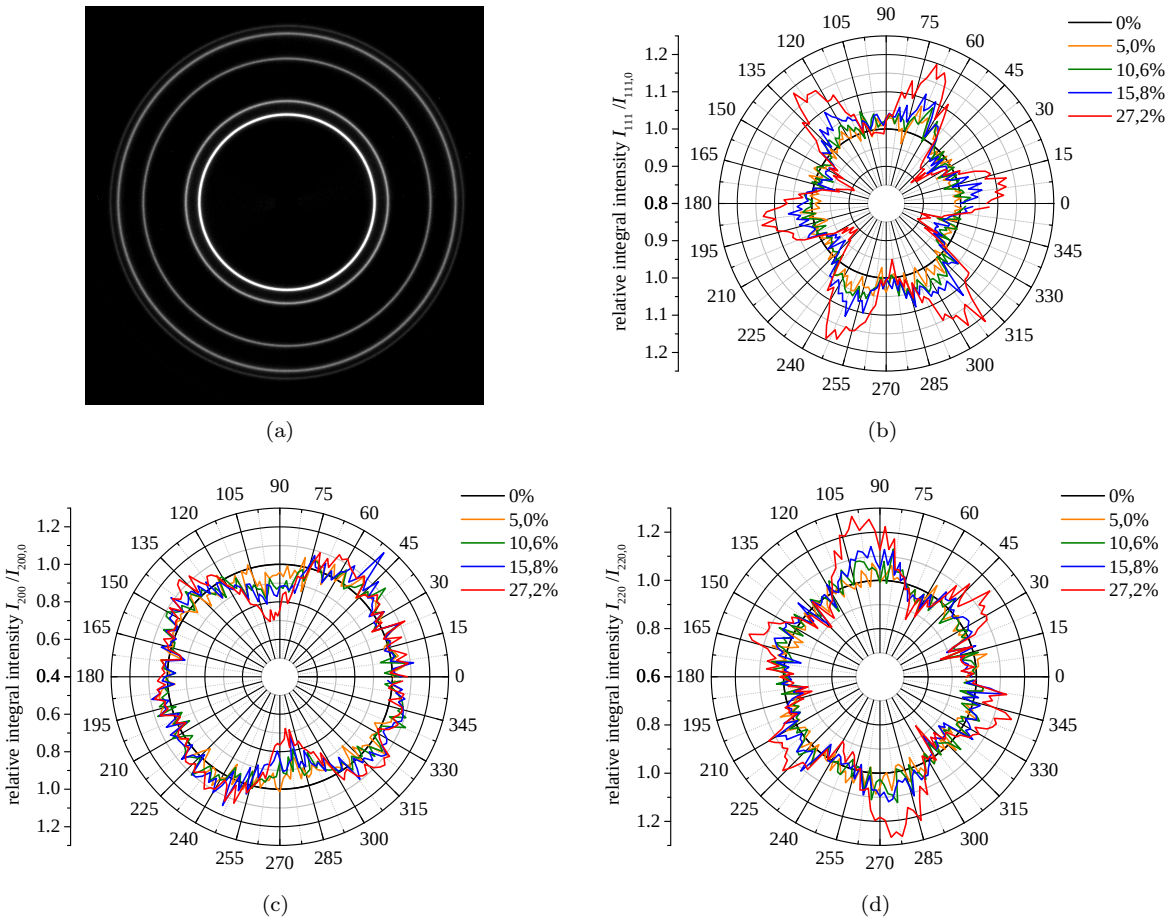

Figure 7: (a) Picture of the detector signal of the initially undeformed NC sample, showing uniformly distributed intensities along the Debye-Scherrer-rings, typical for the scattering of homogeneous and isotropic polycrystals. (b-d) Polar plots of integral scattering intensities at five selected deformation states ((b) {111}, (c) {200} and (d) {220}). Actually, relative intensities I/I_0 normalized by the initial scattering intensity I_0 of the undeformed SCS are shown to emphasize subtle intensity changes.

revolutions. Their samples were also prepared by IGC, employing the same processing protocol as discussed in section 2. They utilized position-sensitive x-ray microdiffraction equipped with an Eulerian cradle and a two-dimensional detector on a lab diffractometer operated in reflection geometry (CuK_α – radiation, $\lambda = 1.542\,\text{Å}$). With shifting the diffraction spot radially outwards, increasingly strained sample sites could be probed. For strains up to $\gamma \approx 1$, they observed a random texture undistinguishable from that of the undeformed sample state and so argued that GB-mediated processes must carry the deformation without leading to texture formation. At larger strain values ($1 < \gamma < 17$), the evolution of a "brass-type" texture which mainly consists of $B/\bar{B}$ simple shear components has been observed. Texture modeling revealed that best agreement with experiment is obtained by referring to the Taylor model in conjunction with the $\{111\}\langle 112\rangle$ slip system family which is by far dominating strain propagation. Moreover, they argue that slip should relate to nucleation and emission of $1/6\langle 112\rangle$ partial dislocations from GB sources. Generally, slip of such partials should generate stacking faults in the grains. However, by peak profile analysis they found that stacking faults and twins existing have a rather low density. As a result, they concluded that intrinsic stacking faults become eventually eliminated by a time-shifted trailing partial emitted from the same GB source. Summarizing the central results: First, it is found that GB-mediated deformation is the effective carrier of strain, even when strains reach out to $\gamma \approx 1$; concomitant texture formation has not been detected.

Secondly, a texture consisting of the $B/\bar{B}$ simple shear components (brass-type texture) has been found to evolve in the strain regime $\gamma > 1$. Texture modeling based on the Taylor model suggests slip related to the $\{111\}\langle 112\rangle$ slip system family best agrees with the observed texture. Thirdly, stacking fault formation is a rare event, likewise, a volume contribution of mechanical twinning to strain is negligible.

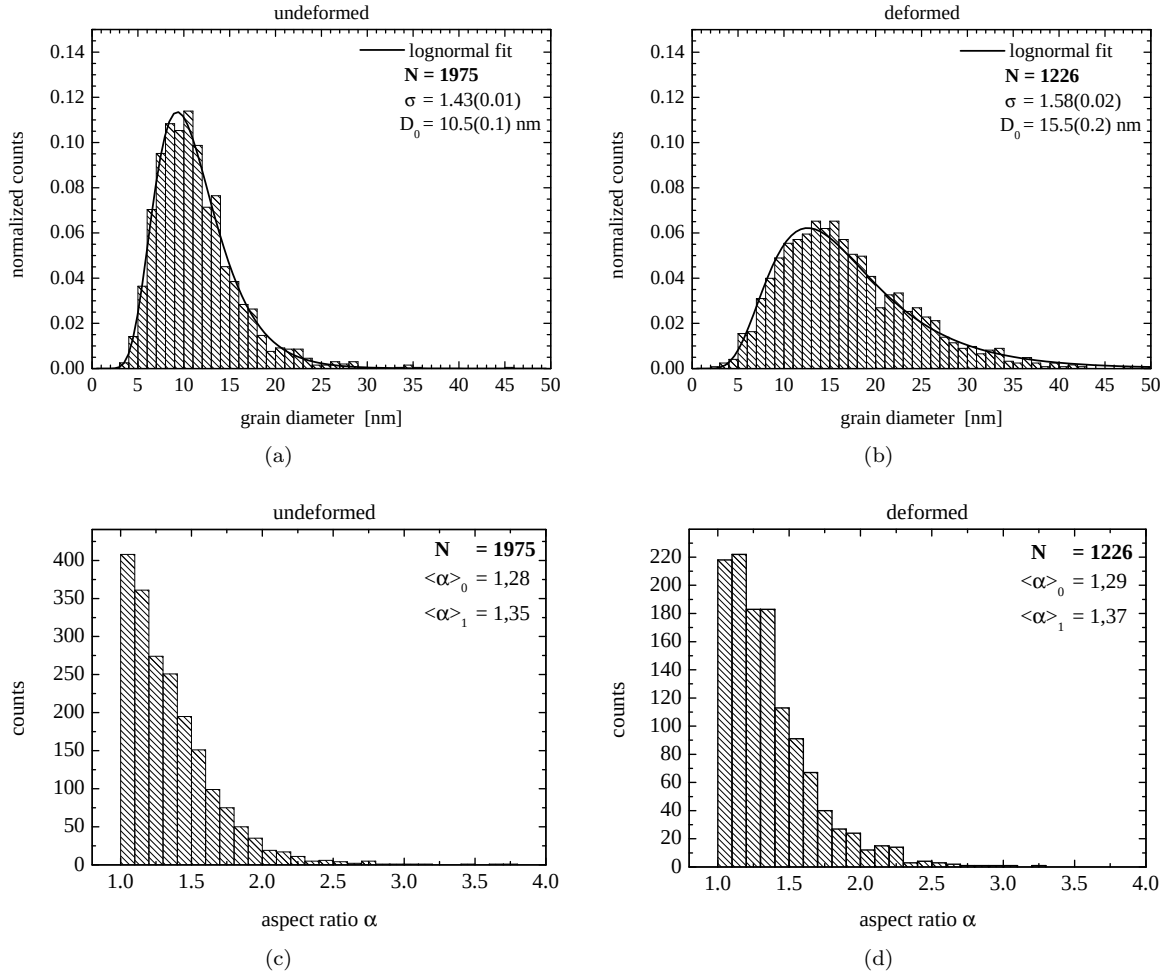

Figure 8: Grain size and aspect ratio distributions of a $Pd_{90}Au_{10}$-SCS measured by TEM. (a, c) Undeformed sample (b, d) gauge section deformed to 32 % applied strain. A log-normal distribution was fitted to the grain diameter histograms to find the median D_0 and distribution width σ. In case of the aspect ratio, the median $\langle\alpha\rangle_0$ and the arithmetic mean $\langle\alpha\rangle_1$ were calculated directly from the histogram. In all cases, N denotes the number of counted grains.

To characterize the possible deformation-induced change of aspect ratio, we measured the grain diameters along the short and long axis of the cross-section of individual grains in TEM dark-field micrographs of thin lamellae, taken from the undeformed part of a SCS and its gauge section having experienced 32 % applied strain (for details see section 2). The so recorded data are displayed in Fig. 8. The aspect ratio histogram of the undeformed material is shown in Fig. 8(c), and the histogram of the plastically deformed gauge section is presented in Fig. 8(d). As expected, we observe an only small change of the arithmetic mean vlaue of the aspect ratio distributions of the undeformed ($\langle\alpha\rangle_1 \approx 1.35$) and deformed ($\langle\alpha\rangle_1 \approx 1.37$) material. Change of aspect ratio and its relation to generation of shear strain through dislocation glide will be discussed in the next paragraph.

Assessing shear strain through dislocation glide requires to estimate the number of dislocations having traversed a grain with the idea that each dislocation incrementally contributes to the change of aspect

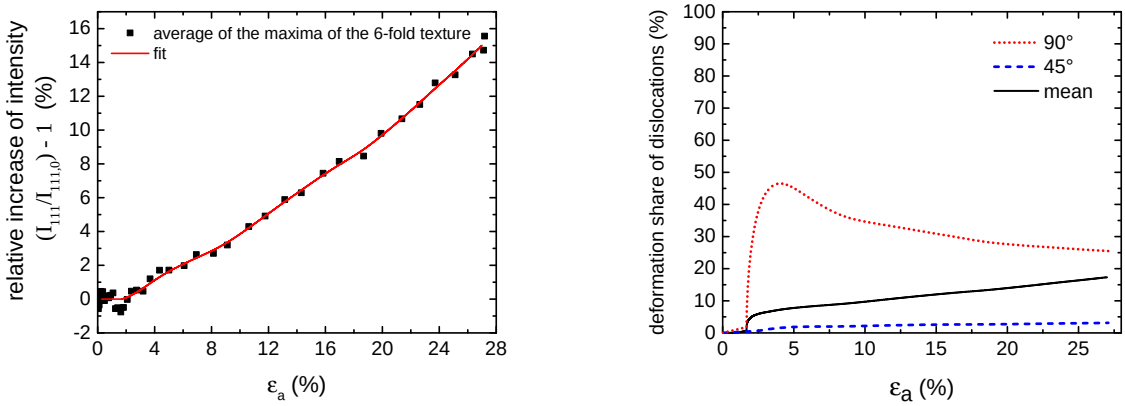

(a) (b)

Figure 9: (a) Average increase of the {111}-scattering intensity at the maxima in Fig. 7(b). The red line is a smoothing spline fit to the data. (b) Dislocation share for different starting angles φ of sheared ellipses. The mean value is averaged over $0° \leq \varphi \leq 90°$ and corresponds to a random distribution of starting angles.

ratio (grain elongation along the glide direction and shrinkage in the respective perpendicular direction). If a number n of full dislocations (or pairs of partials) traverses a crystallite of equivalent diameter D, it is sheared by $n \cdot b$, where $b = 0.275\,\mathrm{nm}$ is the length of the Burgers vector. This causes a shear strain $\gamma\,(n, D) \approx nb/D$ respectively the related plastic strain $\varepsilon_{\mathrm{p,dis}}\,(n, D) = \gamma/\sqrt{3}$ [42]. Estimating the associated change of aspect ratio α of the grain relies upon the grain geometry. Since basically we apply simple shear, let us assume for the sake of simplicity that the initially undeformed grain can be represented by its two dimensional cross section. We further simplify matters by approximating the cross section by an ellipse with semi-major axis A and semi-minor axis B; this geometry is commonly used by automated crystal orientation mapping by means of TEM (ACOM-TEM) [43, 44] to represent grain shape information. Complying with the definition of grain size D, the ellipse has identical area as a circular grain with diameter D, i.e. $\pi D^2/4 = \pi AB$ and the aspect ratio α is defined as $\alpha = A/B$.

Using cartesian coordinates, a sheared ellipse, with its center at the origin ($x = y = 0$), is represented by the following parametric equation

$$\vec{E}(t) = \begin{pmatrix} x(t) \\ y(t) \end{pmatrix} = \begin{pmatrix} A\cos(t)\cos(\varphi) - B\sin(t)\sin(\varphi) \\ A\cos(t)\sin(\varphi) - B\sin(t)\cos(\varphi) \end{pmatrix} + \begin{pmatrix} 0 \\ \frac{b\cdot n}{A}\left(A\cos(t)\cos(\varphi) - B\sin(t)\sin(\varphi)\right) \end{pmatrix} \quad (5)$$

with the parameter $t \in [0, 2\pi]$ and φ which is the angle between the x-axis and the semi-major axis. The left term represents the unsheared ellipse, and the right term accounts for shearing of the ellipse in y-direction by n full dislocations. The quantity $\left|\vec{E}(t)\right|$ denotes the distance between a point on the contour of the ellipse, specified by t, and the origin of the coordinate system. Therefore, the maximum and minimum of $\left|\vec{E}(t)\right|$ straightforwardly provide the length of the semi-major and semi-minor axes of the sheared ellipse, which then allows us to compute the shear-dependent aspect ratio α. Additionally, we can define the shear-induced rotation angle β, being the angle between the semi-major axis of the unsheared and sheared ellipse. We compute β as $\beta = \arctan\left(y(t_{\max})/x(t_{\max})\right) - \varphi$, where $t_{\max}$ specifies the parameter t which belongs to the semi-major axis of the sheared ellipse.

In order to model the evolution of the mean aspect ratio ($1.35 \leq \langle\alpha\rangle_1 \leq 1.37$), we assume that the increase is proportional to the evolution of the relative integral scattering intensity of the {111}-reflex (Fig. 9(a)). As a result, applied strain ε_{a} can be correlated with the mean aspect ratio $\langle\alpha\rangle_1$ and the number of dislocations n. However, as shown in Fig. 5(c), the grain size changes simultaneously during deformation,

which not only affects the strain caused by dislocations $\varepsilon_{\mathrm{p,dis}}(n, D)$ but additionally the length of the semi-major and semi-minor axes. To account for these correlations, we chose an iterative approach where an ellipse is stepwise sheared in y-direction by 1 % of the length of a Burgers vector. After each shear increment, the resulting aspect ratio α and rotation β are computed and correlated with the total applied strain ε_{a} and grain size D. With this set of parameters a new ellipse is created which then experiences the next shear increment. This procedure is repeated N-times, where $N = 100 \cdot n$ and n is chosen in such a manner that the full range of applied strain ε_{a} is covered. The total strain due to dislocation glide for a given number of dislocations, $\varepsilon_{\mathrm{p,dis}}(n)$, is the sum of the strains accumulated during $N(n)$ steps. We note that the strain contributed by dislocation glide, $\varepsilon_{\mathrm{p,dis}}(n)$, no longer depends on D explicitly, as in the described iterative approach D is treated as an n-dependent quantity.

The central result of this analysis reveals that the initial orientation of the unsheared ellipse relative to the direction of shear has a tremendous impact on the number of dislocations needed to reach a given change in aspect ratio α and, therefore, amount of strain caused by dislocation glide or likewise its contribution to total applied strain $\varepsilon_{\mathrm{p,dis}}/\varepsilon_{\mathrm{a}}$. The limiting cases ($\varphi = 90°$ and $\varphi = 45°$) are shown in Fig. 9(b). To estimate the true contribution of dislocations to the total applied strain, we average over a random distribution of grain shape orientations $\varphi \in [0°, 90°]$, which is sampled in 0.5 ° steps. The resulting mean share of dislocation glide is shown in Fig. 9(b) and reveals an abrupt increase at $\varepsilon_{\mathrm{a}} \approx 2\,\%$ followed by a sluggish monotonic increase. Below $\varepsilon_{\mathrm{a}} = 11\,\%$ the dislocation share contributes less than the elastic lattice strain to the total deformation and even at the highest strain in the experiment $\varepsilon_{\mathrm{a}} = 27\,\%$, its contribution to overall strain does not exceed 20 %. It should be noted that this estimate represents an upper bound to the number of dislocations and plastic shear because the change in aspect ratio is exclusively attributed to dislocation activity.

The ellipse approach discussed above relies on the shear strain induced change of aspect ratio of a freestanding ellipse relative to its unstrained configuration. This change of aspect ratio causes a rotation of the semi-major axis of the ellipse. However, free rotation of grains in a polycrystal is impeded by compatibility constraints exerted by neighbouring grains. Hence, it is implied that the orientation of the semiaxes of a grain that experiences deformation in a polycrystalline environment remains rather fixed. Adopting the ellipse approach to this realistic scenario thus requires a reinterpretation.

For the sake of argument and in view of the comparatively moderate applied strain, we assume that the change of aspect ratio of the ellipse occurs at a fixed orientation of semiaxes. The concomitant rotation $\langle\beta\rangle$ is then associated with a rotation of the crystal lattice inscribed to the ellipse through shear by dislocation glide. With this supposition, we find an angle $\langle\beta\rangle \approx 4°$ of mean lattice rotation. This mean value represents an upper bound estimate since we neglect any shape reorientation. The central result of this reinterpretation can even be tested against experiment. Kobler used ACOM-TEM to measure grain rotations in strained NC PdAu thin films to find a spectrum of grain rotations which fell in the angular regime below 10°. It is crucial to note that such rotations were only detected in such cases where grains had a high Schmid-factor [44]. Therefore, the origin of these weak grain rotations has been attributed to dislocation plasticity. Remarkably, the vast majority of such grains rotated less than 4°, which is in line with our upper bound estimate for mean lattice rotation through shear by dislocation glide. Finally, we arrive at the conclusion that our analysis of mean lattice rotation lends independent support to the validity of the results derived from the ellipse approach. Consequently, the share of dislocation activity to overall strain as displayed in Fig. 9(b) may be seen as a manifestation of the identified weak lattice rotations.

Interestingly, *Bachurin* et al. [40] carried out atomistic simulations of uniaxial tensile and compressive loading of NC Pd with a mean grain size of 10 nm. They came to the conclusion that the contribution of extended partial dislocations emitted from the GBs as well as full dislocations and twinning (at later stages of deformation) to the total strain is insignificant. Summing up over all sorts of dislocation contributions including dislocation embryos, they found at a total strain of $\approx 10\,\%$ a relative share of dislocation-based deformation of about 10 %.

As a summary of this section, we conclude that in NC metals with a mean structural correlation length of 10 nm dislocations rather serve as carriers of accommodation processes instead of acting as generic flow defect which propagates strain in a dominant manner.

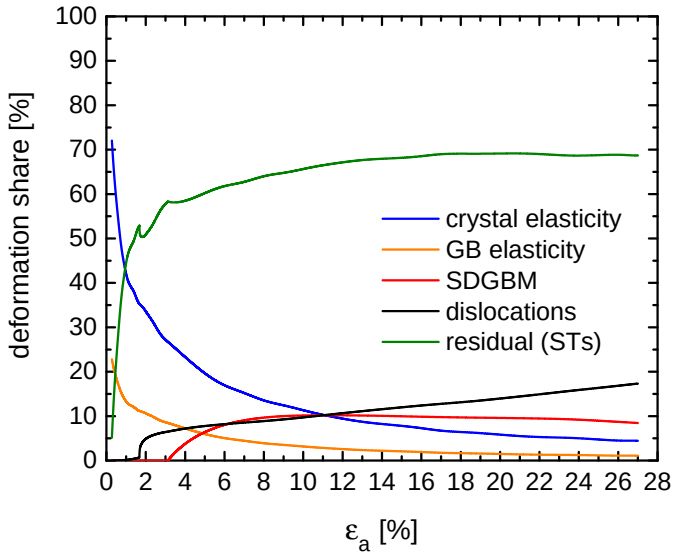

Figure 10: Contributions of different deformation mechanisms relative to the applied strain ε_a. The green line shows the evolution of the residual share, which we assign to ST-induced accumulation of shear strain at/along GBs.

4. Conclusions

In the previous sections we identified four different strain carrying mechanisms as well as their relative contributions to overall deformation, which are altogether displayed in Fig. 10. In addition to the elastic, dislocation based, and SDGBM strain shares, we also show the difference between the sum of these shares and 100 % strain contribution. Strikingly, this residual contribution, steeply rising in the early stage of deformation, approaches a strain share of more than 60 % implying that about two thirds of total deformation are yet unaccounted for. Since x-ray diffraction is particularly sensitive to microstructural changes associated with deviations from perfect intracrystalline order but is non-sensitive to intercrystalline interference, it seems self-evident that the unaccounted strain contribution must have been propagated by GB-mediated deformation modes. The core structure of GBs and possible deformation-induced configurational changes of GB cores give rise to diffuse scattering but its analyis is highly involved and therefore beyond the scope of this study.

In a recent work [15], we have been led to the same conclusion, however, based on reverse reasoning. By deriving expressions for the *effective* activation volume and utilizing experimental or theoretical values for the specific activation volumes of the involved deformation mechanisms, we estimated the relative contributions of deformation modes to arrive at a share of GB-mediated deformation through ST-activity of $\approx 70\,\%$. We note that the GB-mediated deformation share obtained from in-situ deformation and diffraction has lower bound character in strict sense, insofar both ways of reasoning agree. From the determination of the effective activation energy and its stress dependence [15], we concluded that shear transformations (STs), the generic flow event in metallic glasses, must operate in/at GBs. We notice that in contrast to metallic glasses, where emerging STs will eventually self-organize to form macroscopic shear bands, the topology and connectivity of GBs effectively impede the emergence of shear bands and thus prevent the material from stick-slip behavior or catastrophic failure (Fig. 2). Based on this independent evidence, it seems justified now to maintain that STs, emerging in the core region of GBs, account for about two thirds of total strain in NC $Pd_{90}Au_{10}$ at the low end of the nanoscale ($D \lesssim 10\,\mathrm{nm}$). Likewise, in a recent study [32] we demonstrated that plastic yielding in NC Pd-Au alloys mimics universal behavior of metallic glasses, entailing a linear correlation between shear strength and shear modulus. As a consequence, one observes solid solution softening of NC Pd-Au alloys

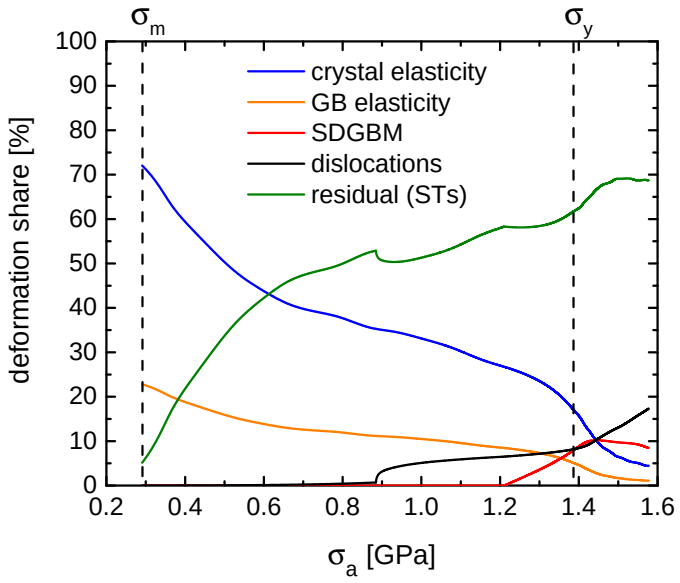

Figure 11: Contributions of different deformation mechanisms relative to the applied stess σ_a. Just like in Fig. 10, the green line shows the evolution of the residual share, which we assign to ST-mediated deformation.

(mean grain size $\lesssim 10\,\mathrm{nm}$) with increasing Au-concentration in contrast to hardening seen in the coarse grained counterparts. We, therefore, suggested that STs rather than dislocations are the dominant carriers of strain in the fully miscible NC $Pd_xAu_{1-x}, 100 < x < 50$, alloy system. In fact, predictions of the change of strength of the NC Pd-Au alloy system, which have been derived from available dislocation-based models and theories, could be disproved without exception.

In the pertinent literature dealing with nanoplasticity, GB-mediated deformation frequently becomes associated with GB sliding. This term has been originally introduced to denote the rigid body translation of abutting crystallites along a shared interface that produces offsets in marker lines at the GBs. The two classical modes of GB sliding comprise Rachinger sliding, which must be accommodated by intragranular dislocation glide and climb, and Lifshitz sliding that is based on stress-directed diffusion of vacancies and is self-accommodating. These sliding modes occur under creep conditions at elevated temperatures and are characterized by strain-rate sensitivities > 0.3 and activation volumes $< 0.1\,\mathrm{b}^3$, respectively. By comparison with activation parameters from our previous work [15], GB sliding can be ruled out being active in the NC materials at the given testing conditions. In line with this reasoning, Wu et al. [21] deduced from computer simulation on NC Ni that the occurence of rigid body translation of grains is related to the system size. When it is not large enough, the proximity of free surfaces reduces the constraint exerted by surrounding grains so favoring easy sliding; the opposite is true for increasing system size. Thus, they argued that in realistic NC microstructures GB sliding is kinematically constrained by triple junction lines and quadrupole points. Nevertheless, STs evolving in the core region of GBs are not hampered by these constraints, in fact, their occurence becomes even facilitated since the shear modulus of GBs in NC metals is reduced by $30\,\% - 50\,\%$ [34, 32] compared to the respective bulk values. On the other hand, dislocation shear, which is nucleation controlled at the low end of the nanoscale [40], therefore, should exert comparatively larger resistance to shear deformation. For that reason, we prefer to assign the irreversible shear strain accumulated along/at GBs to STs and omit the term GB sliding to avoid confusion with nomenclature in what follows. We finally notice that the activity of STs in the core region of GBs genuinely allows for translational and rotational degrees of freedom of grains relative to each other and so is not in conflict with the emergence of displacement discontinuities across/along GBs to maintain compatibility.

In Fig. 11, we display the shares of the different mechanisms as a function of applied stress to unravel their

simultaneous and/or sequential onset and persistence. For convenience, we also designate the characteristic stress values extracted from yield criteria applied in the stress-strain domain [14]: σ_m marks the deviation from linear stress-strain behavior, the onset of so-called microplasticity, and σ_y denotes the yield stress, agreeing with the stress value at which the applied strain rate approaches the materials intrinsic plastic strain rate. We omit the data below σ_m since sample mounting problems generated uncertainties in this regime of the load displacement curves (see section 2). To nevertheless shed light on this deformation stage, computer simulations unraveled that loading a specimen along a perfectly linear stress-strain trajectory ($\sigma < \sigma_m$) does not necessarily imply presence of Hookean elasticity. Bachurin et al. [45] demonstrated that unloading a sample in the *apparent* elastic regime already results in non recoverable inelastic strain which amounts to $0.1 - 0.15\%$ at an applied strain of 1%. This observation is consistent with our finding that the share of the residual contribution in Fig. 11 assumes a small but finite value at σ_m.

In the stress regime $\sigma_m < \sigma_a < \sigma_y$ the deformation behavior is dominated by Hookean elasticity of the grains and GBs as well as shear shuffling (STs) taking place in the core region of GBs. We observe a rather abrupt onset of dislocation activity at around 0.9 GPa followed by a rather weak increase up to σ_y. The onset of SDGBM starts out at around 1.2 GPa to approach a maximum slightly above σ_y. Interestingly, the yield stress determined by prescribing that the imposed strain rate compares with the intrinsic plastic strain rate obviously ensures that the full set of deformation modes is active at σ_y. Ignoring for the sake of argument the contributions of SDGBM and dislocations which become effective above ≈ 1.0 GPa, our finding has two profound implications. First, GB-mediated deformation by STs is capable of propagating plastic strain without assistance/interplay of simultaneously acting and irreversible deformation carrying accommodation mechanisms. This behavior is in particular relevant in the stress regime below 1.0 GPa. When analyzing the activation energy of shear shuffling, Grewer et al. had to explicitly assume that the activity of STs is *not* coupled to accommodation mechanisms with activation energies distinctively deviating from activation of STs. The identified sole activity of STs acting as carriers of inelastic strain and their evolution to become the dominant strain carrier at large strain thus a posteriori justify the presumption made in [15]. Secondly, the conventional concept of work or strain hardening that essentially refers to intracrystalline dislocation interactions seems not being applicable here. This notion also coincides with the analysis of the strain-rate dependence of stress in [15], where it could be verified that the material response in the stress regime $\sigma_m < \sigma_a < \sigma_y$ agrees with nonlinear viscous behavior.

When $\sigma_\mathrm{a} > \sigma_y$ the share of SDGBM runs through a maximum to then decrease, whereas, dislocation activity gains progressively more influence to develop the largest rate of increase when the largest stress values are reached. Hookean lattice elasticity tends to assume the minimum share ($\approx 5\%$) here and STs carry a strain share of about 70%. It seems conceivable that SDGBM and dislocation glide may interact in a synergistic manner e.g. through enhanced grain growth and concomitant increasing intracrystalline dislocation activity at local stress concentrations thereby avoiding early brittle fracture. Overall, the diverse evolution of the respective deformation shares appears as being just a consequence of a complex hierarchical order of onset/nucleation and upholding stresses of different deformation mechanisms, the presence and degree of activity of which strongly depends on grain size. For example, in a recent study of NC Ni with a grain size of 30 nm, a strain share of about 40 % could be assigned to dislocation activity [31]. We finally conjecture that the state of the GB core structure, whether in relaxed (low-excess-energy) or as prepared (high-excess-energy state) configuration, should also have a decisive effect on the share and onset stresses of the above discussed deformation modes. Furthermore, the stacking fault energy of the Pd-Au alloys decreases with rising Au concentration [25, 26] and, therefore, partial dislocation activity should increase towards Au-rich alloys. Consequently, we expect that alloy composition may influence the magnitude of the dislocation share.

5. Summary

In this work, we have utilized in-situ diffraction and post mortem microscopy in conjunction with dominant shear deformation to identify, dissect, and quantify the relevant deformation mechanisms in nanocrystalline (NC) $Pd_{90}Au_{10}$ in the limiting case of $D \lesssim 10$ nm. We could identify lattice and grain boundary (GB) elasticity, shear shuffling or shear transformations (STs) operating in the core region of GBs, stress driven

grain boundary migration (SDGBM), and dislocation shear along lattice planes to all contribute, however, with significantly different and non-trivial stress-dependent shares to overall deformation. The frequently used term GB sliding has been discarded here since STs, which act as generic flow event in metallic glasses, have been unambigiously identified to also operate as dominant strain carriers in the core region of GBs [15].

It was not required to invoke nonlinear elasticity to adequately describe the material response. In the so-called microplastic regime, STs coexist with lattice- and GB elasticity in a way that the share of the latter decreased inversely proportional to the progressive increase of STs. Dislocation activity contributes with a share of less than 10% in this regime, implying that it rather acts as accommodation mechanism. As a matter of fact, STs and elastic contributions by far dominate the material response in this regime, therefore, it seems plausible to discard the conventional concept of work- or strain hardening to account for the evolution of the tangent modulus. This assessment is consistent with a recent finding unveiling that NC Pd-Au alloy-systems manifest solid solution softening at the low end of the nanoscale [32] and not dislocation-based hardening behavior.

Moreover, STs which propagate strain at/along GBs have been found to carry about two thirds of the overall strain in the regime of macroplasticity (beyond the yield stress). SDGBM exhibits an appreciable decrease of activity in this regime, whereas dislocation activity progressively increases. Overall, the diverse evolution of the respective deformation shares appears as being just a consequence of a complex hierarchical order of onset/nucleation and upholding stresses of different deformation mechanisms. We expect that the configurational state of the material's microstructure, whether tested in as prepared or relaxed state, should have a decisive influence on this hierarchy.

6. Acknowledgment

The authors are grateful for the preparation of the FIB lamellae and TEM dark field micrographs taken by Aaron Kobler at the Karlsruhe Micro Nano Facility (KMNF), the MPI-Stuttgart for access to the High Energy Micro-Diffraction apparatus at ID15/ESRF, as well as the synchrotron beamtime provided by the European Synchrotron Radiation Facility (ESRF experiments MA1112 & MA1353), and financial support from DFG (FOR 714 and BI 385/18-1). The authors also want to thank Andreas Leibner for fruitful discussions, as well as assistance with data reduction.

References

[1] M. A. Meyers, A. Mishra, D. J. Benson, Mechanical properties of nanocrystalline materials, Prog. Mater. Sci. 51 (2006) 427–556.
[2] M. Dao, L. Lu, R. J. Asaro, J. T. M. De Hosson, E. Ma, Toward a quantitative understanding of mechanical behavior of nanocrystalline metals, Acta Mater. 55 (2007) 4041 – 4065.
[3] N. Q. Vo, R. S. Averback, P. Bellon, A. Caro, Limits of hardness at the nanoscale: Molecular dynamics simulations, Phys. Rev. B 78 (2008) 241402.
[4] H. Van Swygenhoven, P. M. Derlet, Grain-boundary sliding in nanocrystalline fcc metals, Phys. Rev. B 64 (2001) 224105.
[5] J. Weissmüller, J. Markmann, M. Grewer, R. Birringer, Kinematics of polycrystal deformation by grain boundary sliding, Acta Mater. 59 (2011) 4366–4377.
[6] J. W. Cahn, Y. Mishin, A. Suzuki, Coupling grain boundary motion to shear deformation, Acta Mater. 54 (2006) 4953–4975.
[7] J. W. Cahn, J. E. Taylor, A unied approach to motion of grain boundaries, relative tangential translation along grain boundaries, and grain rotation, Acta Mater. 52 (2004) 4887–4898.
[8] M. Legros, D. S. Gianola, K. J. Hemker, In situ tem observations of fast grain-boundary motion in stressed nanocrystalline aluminum films, Acta Mater. 56 (2008) 3380 – 3393.
[9] A. C. Lund, C. A. Schuh, Strength asymmetry in nanocrystalline metals under multiaxial loading, Acta Mater. 53 (2005) 3193–3205.
[10] A. S. Argon, S. Yip, The strongest size, Philos. Mag. Lett. 86 (2006) 713–720.
[11] A. S. Argon, Plastic deformation in metallic glasses, Acta Metall. 27 (1979) 47–58.
[12] P. Gu, M. Dao, R. J. Asaro, S. Suresh, A unified mechanistic model for size-dependent deformation in nanocrystalline and nanotwinned metals, Acta Mater. 59 (2011) 6861 – 6868.
[13] R. J. Asaro, S. Suresh, Mechanistic models for the activation volume and rate sensitivity in metals with nanocrystalline grains and nano-scale twins, Acta Mater. 53 (2005) 3369 – 3382.

[14] M. Ames, M. Grewer, C. Braun, R. Birringer, Nanocrystalline metals go ductile under shear deformation, Mater. Sci. Eng., A (2012) 248–257.
[15] M. Grewer, R. Birringer, Shear shuffling governs plastic flow in nanocrystalline metals: An analysis of thermal activation parameters, Phys. Rev. B 89 (2014) 184108.
[16] W. L. Johnson, K. Samwer, A universal criterion for plastic yielding of metallic glasses with a $(t/T_g)^{2/3}$ temperature dependence, Phys. Rev. Lett. 95 (2005) 195501.
[17] W. Skrotzki, A. Eschke, B. Jóni, T. Ungár, L. Tóth, Y. Ivanisenko, L. Kurmanaeva, New experimental insight into the mechanisms of nanoplasticity, Acta Mater. 61 (2013) 7271 – 7284.
[18] H. Van Swygenhoven, P. M. Derlet, A. G. Frøseth, Nucleation and propagation of dislocations in nanocrystalline fcc metals, Acta Mater. 54 (2006) 1975 – 1983.
[19] V. Yamakov, D. Wolf, S. R. Phillpot, A. K. Mukherjee, H. Gleiter, Deformation-mechanism map for nanocrystalline metals by molecular-dynamics simulation, Nat. Mater. 3 (2004) 43–47.
[20] N. Q. Vo, R. S. Averback, P. Bellon, S. Odunuga, A. Caro, Quantitative description of plastic deformation in nanocrystalline cu: Dislocation glide versus grain boundary sliding, Phys. Rev. B 77 (2008) 134108.
[21] Z. Wu, Y. Zhang, M. Jhon, D. Srolovitz, Anatomy of nanomaterial deformation: Grain boundary sliding, plasticity and cavitation in nanocrystalline ni, Acta Mater. 61 (2013) 5807–5820.
[22] R. Birringer, Nanocrystalline materials, Mater. Sci. Eng. A 117 (1989) 33 – 43.
[23] R. Birringer, M. Hoffmann, P. Zimmer, Interface stress in nanocrystalline materials, Z. f. Metallk. 94 (2003) 1052–1061.
[24] C. E. Krill, R. Birringer, Estimating grain-size distributions in nanocrystalline materials from x-ray diffraction profile analysis, Phil. Mag. A 77 (1998) 621–640.
[25] J. Schäfer, A. Stukowski, K. Albe, Plastic deformation of nanocrystalline pd-au alloys: On the interplay of grain boundary solute segregation, fault energies and grain size, Acta Mater. 59 (2011) 2957 – 2968.
[26] Z. Jin, S. Dunham, H. Gleiter, H. Hahn, P. Gumbsch, A universal scaling of planar fault energy barriers in face-centered cubic metals, Scr. Mater. 64 (2011) 605–608.
[27] H. P. Klug, L. E. Alexander, X-Ray Diffraction Procedures For Polycrystalline and Amorphous Materials, 2. ed., Wiley-Interscience, 1974.
[28] J. Markmann, V. Yamakov, J. Weissmüller, Validating grain size analysis from x-ray line broadening: A virtual experiment, Scipta Mat. 59 (2008) 15–18.
[29] D. Rittel, S. Lee, G. Ravichandran, A shear-compression specimen for large strain testing, Exp. Mech. 42 (2002) 58–64.
[30] M. Ames, J. Markmann, R. Birringer, Mechanical testing via dominant shear deformation of small-sized specimen, Mater. Sci. Eng., A 528 (2010) 526–532.
[31] J. Lohmiller, M. Grewer, C. Braun, A. Kobler, C. Kübel, K. Schüler, V. Honkimäki, H. Hahn, O. Kraft, R. Birringer, P. A. Gruber, Untangling dislocation and grain boundary mediated plasticity in nanocrystalline nickel, Acta Mater. 65 (2014) 295 – 307.
[32] A. Leibner, C. Braun, J. Heppe, M. Grewer, R. Birringer, Plastic yielding in nanocrystalline pd-au alloys mimics universal behavior of metallic glasses, Phys. Rev. B 91 (2015) 174110.
[33] J. Weissmüller, J. Cahn, Mean stresses in microstructures due to interface stresses: A generalization of a capillary equation for solids, Acta Materialia 45 (1997) 1899 – 1906.
[34] M. Grewer, J. Markmann, R. Karos, W. Arnold, R. Birringer, Shear softening of grain boundaries in nanocrystalline pd, Acta Mater. 59 (2011) 1523 – 1529.
[35] T. Ungár, G. Tichy, The effect of dislocation contrast on x-ray line profiles in untextured polycrystals, Phys. Stat. Sol. (a) 171 (1999) 425–434.
[36] A. Stukowski, J. Markmann, J. Weissmüller, K. Albe, Atomistic origin of microstrain broadening in diffraction data of nanocrystalline solids, Acta Materialia 57 (2009) 1648 – 1654.
[37] M. Ames, J. Markmann, R. Karos, A. Michels, A. Tschöpe, R. Birringer, Unraveling the nature of room temperature grain growth in nanocrystalline materials, Acta Mater. 56 (2008) 4255–4266.
[38] T. H. de Keijser, J. I. Langford, E. J. Mittemeijer, A. B. P. Vogels, Use of the voigt function in a single-line method for the analysis of x-ray diffraction line broadening, J. Appl. Crystallogr. 15 (1982) 308–314.
[39] I. A. Ovid'ko, A. G. Sheinerman, Special strain hardening mechanism and nanocrack generation in nanocrystalline materials, Appl. Phys. Lett. 90 (2007) 171927.
[40] D. Bachurin, P. Gumbsch, Accommodation processes during deformation of nanocrystalline palladium, Acta Mater. 58 (2010) 5491 – 5501.
[41] D. Molodov, T. Gorkaya, G. Gottstein, Dynamics of grain boundaries under applied mechanical stress, J. Mater. Sci. 46 (2011) 4318–4326.
[42] A. S. Argon, Strengthening Mechanisms in Crystal Plasticity, Strengthening Mechanisms in Crystal Plasticity, Oxford University Press, 2008.
[43] A. Kobler, A. Kashiwar, H. Hahn, C. Kübel, Combination of in situ straining and {ACOM} tem: A novel method for analysis of plastic deformation of nanocrystalline metals, Ultramicroscopy 128 (2013) 68 – 81.
[44] A. Kobler, Untersuchung der Deformationsmechanismen in nanostrukturierten Metallen und Legierungen mit Transmissionselektronenmikroskopie, Ph.D. thesis, Technische Universität Darmstadt, Darmstadt, 2015. URL: `http://tuprints.ulb.tu-darmstadt.de/4432/`.
[45] D. V. Bachurin, P. Gumbsch, Elastic and plastic anisotropy after straining of nanocrystalline palladium, Phys. Rev. B 85 (2012) 085407.